Renewable Energy 102 (2017) 390–405

Contents lists available at ScienceDirect

Renewable Energy

journal homepage: www.elsevier.com/locate/renene

A unified high-resolution wind and solar dataset from a rapidly updating numerical weather prediction model

Eric P. James [a, b, *], Stanley G. Benjamin [a], Melinda Marquis [a]

[a] NOAA Research – Earth System Research Laboratory, 325 Broadway, Boulder, CO, 80305, USA
[b] Cooperative Institute for Research in Environmental Sciences, University of Colorado, 216 UCB, Boulder, CO, 80309, USA

ARTICLE INFO

Article history:
Received 25 June 2016
Received in revised form
6 October 2016
Accepted 27 October 2016
Available online 28 October 2016

Keywords:
Wind resource
Solar resource
NWP forecast
Unified wind/solar

ABSTRACT

A new gridded dataset for wind and solar resource estimation over the contiguous United States has been derived from hourly updated 1-h forecasts from the National Oceanic and Atmospheric Administration High-Resolution Rapid Refresh (HRRR) 3-km model composited over a three-year period (approximately 22 000 forecast model runs). The unique dataset features hourly data assimilation, and provides physically consistent wind and solar estimates for the renewable energy industry. The wind resource dataset shows strong similarity to that previously provided by a Department of Energy-funded study, and it includes estimates in southern Canada and northern Mexico. The solar resource dataset represents an initial step towards application-specific fields such as global horizontal and direct normal irradiance. This combined dataset will continue to be augmented with new forecast data from the advanced HRRR atmospheric/land-surface model.

1. Introduction

Today's global economy depends to a large extent upon a reliable electricity generation and distribution system. In the United States (US) and indeed around the world, traditional power generation technologies such as coal, natural gas, and nuclear energy are gradually being supplemented, and in some cases replaced, by renewable energy generation systems [2,30]. Advancing technology, as well as growing concern over anthropogenic global climate change, is accelerating this transition to increasingly affordable new power-generation systems.

While more desirable in terms of its smaller anthropogenic footprint, renewable energy generation such as wind, solar, tidal, and geothermal power rely on geophysical phenomena that are variable in space and intermittent in time, posing unique challenges to the generation and distribution system. Among renewable resources, the US Department of Energy (DOE) has highlighted wind energy in particular, setting a goal of achieving 20% of the nation's electrical energy from wind by the year 2030 [31,32]. While less variable diurnally than solar energy, wind energy production is still highly dependent upon favorable weather conditions. Grid operators must anticipate so-called “ramp events”, in which the renewable resource (wind or solar) undergoes a large change (either positive or negative) in a short period of time [20].

Since power-generation infrastructure must generally be fixed in location, it is very important for decision makers to have access to the most accurate resource estimates achievable. For wind, resource assessments are typically done using the “measure-correlate-predict” (MCP) method, wherein a short period of wind tower measurements is correlated with a long-term near-surface wind record in order to predict the wind climatology at turbine height [7]. The observation-based turbine-level wind datasets used to identify potential sites for wind power installations are typically brief in duration, and more importantly are very sparse in their spatial coverage. Furthermore, one of the largest practically accessible wind resources within US territory is offshore of the East Coast (particularly in the vicinity of New England; [3,24,27]). Observations in this area are very limited. Satellite-based synthetic aperture radar measurements (e.g. [22]), have shown promise for oceanic regions; however, the associated retrieval techniques involve many assumptions.

Observation-based solar resource assessments take advantage of long-term radiation measurement networks such as the 14-

* Corresponding author. NOAA Research – Earth System Research Laboratory, 325 Broadway, Boulder, CO, 80305, USA.
E-mail addresses: eric.james@noaa.gov (E.P. James), stan.benjamin@noaa.gov (S.G. Benjamin), melinda.marquis@noaa.gov (M. Marquis).

http://dx.doi.org/10.1016/j.renene.2016.10.059

station SURFRAD/ISIS network in the US [4]. Other observation sources include the Cooperative Networks for Renewable Resource Measurements (CONFRRM; [35]), the University of Oregon Solar Radiation Monitoring Laboratory [36], a number of state monitoring networks (such as the Illinois Climate Network; [37]), and observations supporting solar development by private companies. Complementary satellite observations, conventional surface observations, and model analyses and forecasts [26] also play a role in solar resource assessment.

In addition to a number of resource datasets developed by private companies (e.g., 3Tier, SOLARGIS, Meteonorm), the DOE's National Renewable Energy Laboratory (NREL) has developed wind and solar resource maps for the period since the early 1990s. Maps of the long-term average 80-m wind speed over the contiguous US (CONUS), with 2.5-km horizontal resolution, were derived using fine-resolution simulations and validation-based bias corrections [12]. In addition, the National Solar Radiation Data Base (NSRDB), containing data for over 1400 stations, has been developed based on a number of statistical models [34]. Extending this effort for wind resources, Draxl et al. [10] have recently produced a grid integration dataset for wind energy, referred to as the WIND Toolkit, which includes model-derived meteorological data and simulated forecasts for over 100 000 land-based and offshore wind power production sites.

For grid integration studies in a scenario with significant penetration of both wind and solar, it is important to have access to time-matched, gridded wind and solar data, which in turn determine wind and solar generation profiles (e.g., [19,25]). While NREL's wind and solar datasets were derived using state-of-the-art statistical and modeling techniques based on available observations, they have been derived independently of one another, meaning that the wind and solar resource are not necessarily meteorologically consistent when combined. That is, in regions with few observations, the wind and solar resources could evolve independently of one another, without necessarily representing a meteorologically realistic state. In this paper, we present a unified wind and solar dataset derived from a real-time, hourly-updating numerical weather prediction (NWP) model developed by the National Oceanic and Atmospheric Administration (NOAA). Modern NWP systems continue to have both known and unknown errors associated with their data assimilation and modeling components, but they are able to perform increasingly well for diverse meteorological situations (e.g., [6]). Our goal is to compare these new results with the NREL maps over the CONUS land area and offshore regions, and to demonstrate the expanded utility of a physically consistent hourly solar and low-level wind dataset using recent NWP refinements.

Section 2 describes background information for our study: the configuration of the NWP model and its changes during the 3-year period examined here, and some objective statistical verification of the solar and low-level wind forecasts. Section 3 summarizes the development of the archive of model output used for this study, and describes the procedures for calculating the metrics to be shown. Section 4 presents low-level wind results, and Section 5 presents solar results. These results are summarized and discussed in Section 6.

2. Background on the weather model/assimilation system

In this section, we provide background on the NWP system configuration used for this study, and present objective verification of the model's low-level wind and solar forecasts.

2.1. Hourly updating numerical weather prediction system – the HRRR

The NOAA Earth System Research Laboratory (ESRL) Global Systems Division (GSD) has developed a 13-km horizontal grid NWP model called the Rapid Refresh (RAP; [6]). The RAP is run every hour, out to 21 forecast hours, over a domain that covers all of North America. The RAP replaced the earlier smaller domain Rapid Update Cycle (RUC; [5]) as NOAA's operational rapidly-updating forecast system in May 2012. Since 2010, a nested version of the RAP on a 3-km horizontal grid has also been run hourly in experimental mode at GSD, over a domain the covers the entire CONUS; this nested version of the RAP is called the High-Resolution Rapid Refresh (HRRR). The model domains are shown in Fig. 1. An older version of the HRRR was implemented operationally within NOAA in September 2014; however, all of the results presented here are based on the experimental HRRR at ESRL/GSD. The HRRR and RAP use specially developed versions of the WRF-ARW model [28].

Driven by the need for rapidly-updating real-time forecasts, and in a major difference from the NWP-derived meteorological dataset associated with the WIND Toolkit, the RAP and HRRR assimilate many different types of observations on an hourly basis within the data assimilation procedure. Both models use a community-supported data assimilation package, the Gridpoint Statistical Interpolation (GSI), to carry out 3-dimensional hybrid ensemble/variational data assimilation [6,18], combining latest observations with a high-resolution 1-h forecast to create an initial condition for the next model forecast. At the end of the assimilation, a cloud/hydrometeor analysis [6] is carried out based primarily on satellite cloud-top temperature and surface-based ceilometer data.

The HRRR assimilates radar reflectivity observations by applying latent heating specified from 15-min reflectivity observations during the hour prior to the initial time [1]. Conventional observations are then assimilated prior to the launch of the WRF forecast, allowing a much more realistic local representation of the state of the atmosphere near the beginning of the free forecast than can be achieved by initializing from a large-scale analysis (such as the European Centre for Medium-Range Weather Forecasting Interim Reanalysis used by Draxl et al. [10]).

Draxl et al. [10] restarted their simulations monthly (as opposed to hourly for the RAP and HRRR), using scale-selective grid nudging back to the large-scale analysis every 6 h in order to prevent drift. The RAP avoids drift through a partial cycling technique [6] which involves a 6-h parallel spin-up cycle initialized from the Global Forecast System (GFS) every 12 h. Draxl et al. [10] also used WRF-ARW, like the HRRR and RAP, for all of their WIND Toolkit simulations. Table 1 provides an overview of the physical parameterizations refined for and used in the HRRR; for additional details on these schemes and their application for improved near-surface forecast skill, the reader is referred to [6]. In general, the same physics suite has been used for the HRRR since April 2013, with subsequent internal refinements to each scheme.

The WIND Toolkit meteorological dataset aims to represent low-level winds as accurately as possible, whereas RAP and HRRR development is driven by a need for improved real-time forecasts over a wide array of variables for many different applications. This much broader perspective, while possibly resulting in worse forecasts for individual variables, provides a unified forecast product from one NWP system. In this study, rather than reproduce the work of Draxl et al. [10]; we aim to summarize the characteristics of a combined wind and solar dataset, derived from a single, unified NWP model.

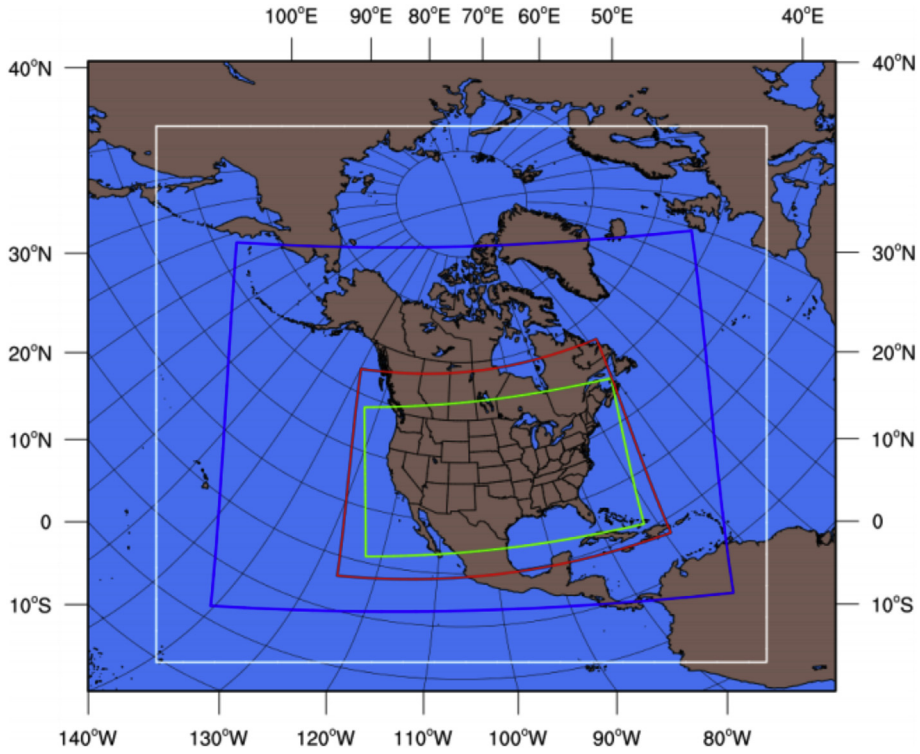

Fig. 1. Map of North America showing the computational domains of the earlier RUC (red), an earlier version of the RAP (blue), the current version of the RAP (white) and the HRRR (green) models. The RAP is on a rotated latitude-longitude grid, and the HRRR is on a Lambert conformal grid. (For interpretation of the references to colour in this figure legend, the reader is referred to the web version of this article.)

Table 1
Important configuration changes within the 3-km HRRR during the 2013–15 period of study, compared to configuration of the 2-km WIND Toolkit WRF model. MYNN: Mellor-Yamada-Nakanishi-Niino. LSM: land surface model. RRTM: Rapid Radiative Transfer Model. RRTMG: Rapid Radiative Transfer Model – Global.

Component	3-km High-Resolution Rapid Refresh	2-km WIND Toolkit
WRF-ARW version	*1 Jan – 30 Mar 2013:* WRFv3.3.1 *30 Mar 2013 – 10 Apr 2014:* WRFv3.4.1 *10 Apr 2014 – 1 Jan 2015:* WRFv3.5.1 *1 Jan – 31 Dec 2015:* WRFv3.6	WRF v3.4.1
Convective scheme/clouds	*1 Jan 2013 – 1 Jan 2015:* None *1 Jan – 31 Dec 2015:* MYNN boundary layer clouds	None
Planetary boundary layer (PBL) scheme	*1 Jan – 4 Apr 2013:* Mellor-Yamada-Janjic *4 Apr 2013 – 10 Apr 2014:* modified version of MYNN *10 Apr 2014 – 1 Jan 2015:* MYNN with reduced thermal roughness over snow *1 Jan – 31 Dec 2015:* further enhanced MYNN	Yonsei Univ. scheme
Land surface model (LSM)	*1 Jan – 13 Mar 2013:* 6-level RUC LSM *13 Mar 2013 – 10 Apr 2014:* 9-level RUC LSM *10 Apr 2014 – 1 Jan 2015:* RUC LSM with increased resolution of top snow layer *1 Jan – 31 Dec 2015:* further enhanced RUC LSM	Noah LSM
Radiation scheme (shortwave)	*1 Jan – 30 Mar 2013:* Dudhia *30 Mar 2013 – 10 Apr 2014:* Goddard (5 min calls) *10 Apr 2014 – 31 Dec 2014:* RRTMG (15 min calls but with solar zenith angle interpolation)	Dudhia
Radiation scheme (longwave)	*1 Jan 2013 – 10 Apr 2014:* RRTM *10 Apr 2014 – 31 Dec 2015:* RRTMG	RRTM
Microphysics scheme	*1 Jan – 30 Mar 2013:* Thompson v3.3.1 *30 Mar 2013 – 10 Apr 2014:* Thompson v3.4.1 *10 Apr 2014 – 4 May 2015:* Thompson v3.5.1 *4 May – 31 Dec 2015:* aerosol-aware Thompson v3.6.1	Eta
Data assimilation (DA) configuration	*1 Jan – 6 Apr 2013:* radar downscaled from the RAP *6 Apr 2013 – 8 Apr 2014:* 15-min radar DA + 3DVar with static model background error covariance *8 Apr 2014 – 31 Dec 2015:* 15-min radar DA + hybrid ensemble/variational DA with 75% flow-dependent covariance from 80-mem GFS ensemble/25% static covariance	None
Cycling	*1 Jan 2013 – 31 Dec 2014:* None *1 Jan – 31 Dec 2015:* land surface only	None

In the remainder of this section, we present quantitative verification results to inform interpretation of the 80-m wind and surface solar results in Section 4. A variety of verification metrics have been used for wind [10] and solar [38] forecasting, but in this study we focus on root mean squared (RMS) error and bias (forecast minus observation). Examining higher-order statistics such as skewness and kurtosis, or measures of ramp performance, represents an effort outside the scope of this work.

2.2. 10-m wind speed verification

Modern wind turbines, often 100–200 m tall, respond to the wind in a layer that is far above any conventional in situ surface-based meteorological observing systems. Thus, wind resource assessments must rely upon observations from dedicated instrumented towers in the vicinity of a potential wind power site. In cases where wind farm development proceeds beyond the initial prospecting phase, these tower anemometer observations often become highly "waked" by the growing number of turbines erected in the surrounding area. This problem precludes the general use of wind tower observations for model verification purposes. In order to circumvent this issue, here we examine 10-m wind verification results using the METAR surface observation network. This network consists of about 1800 stations reporting hourly; exposure of these instruments is generally good, as many of them are located at airports away from tall trees or human-built structures.

In this study, we consider 1-h HRRR forecasts as our best estimate of the state of the atmosphere regardless of the HRRR initialization methods before or after spring 2013 (see Table 1). One-hour forecasts are considered to be close enough to the initial time that the model forecast error is still small and the forecast is still strongly constrained by recent observations. At the same time, the 1-h forecasts are also far enough from the initial time that the model has had time to spin up realistic 3-km structures in the atmosphere consistent with the atmospheric physical processes represented in the HRRR model, which is desirable for this wind/solar dataset. Sufficient adjustment to attain physical consistency with the atmospheric relationships represented in the model, after the arrival of observations in the data assimilation procedure, requires this 1-h forecast duration.

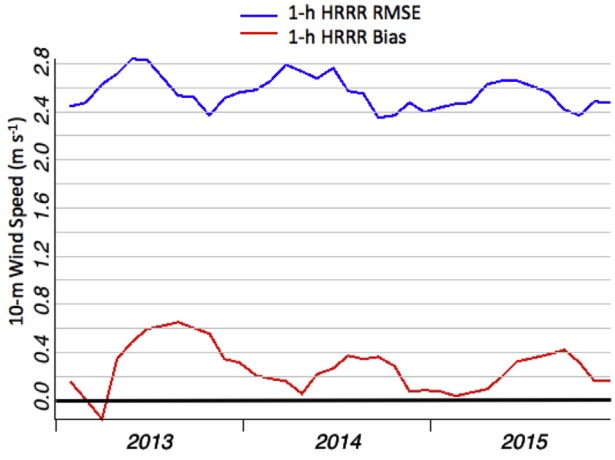

Fig. 2. 10-m wind speed bias (red curve; forecast minus observation; m s^{-1}) and root-mean-squared (RMS) error (blue curve; m s^{-1}) of HRRR 1-h forecasts over the full HRRR domain during 2013–15. Verification is against METAR observations of 10-m wind. A 30-day average is applied to reduce the amount of short-time-scale noise. The thick black line represents an optimal bias of zero. (For interpretation of the references to colour in this figure legend, the reader is referred to the web version of this article.)

Fig. 2 shows the root mean squared (RMS) error and bias (forecast minus observation) of 1-h forecasts of 10-m wind speed from the HRRR, as verified against METAR stations over the entire HRRR domain. Values are averaged over 30-day periods to reduce the amount of noise. It is seen that 1-h forecasts have become increasingly unbiased over the three-year period of study, with positive biases staying below about 0.4 m s^{-1} over the past two years. During the same time period, RMS error has been exhibiting a similar decrease from a maximum of about 2.8 m s^{-1} in late spring 2013 to a minimum of about 2.4 m s^{-1} in autumn 2014. These results suggest that, while 1-h HRRR forecasts continue to have a slight positive wind speed bias at 10 m, the magnitude of the bias has been decreasing, and now resides within 0.5 m s^{-1} of zero.

2.3. 80-m wind speed verification

NREL operates a wind energy technology research facility at the base of the eastern foothills of the Colorado Front Range known as the National Wind Technology Center (NWTC); within this complex are a number of instrumented tall towers for wind measurement. One of these towers, referred to as M2 [14], measures wind speed and direction at 80 m above ground level, providing a potential dataset for verification of the HRRR forecasts that is not waked by a dense network of wind turbines. The M2 tower is located at 39° 54' 38.34 north latitude and 105° 14' 5.28 west longitude, and at an elevation of 1855 m above sea level. For the purposes of this study, we did not undertake any quality control on the dataset; however, the raw observations are considered to be of fairly high quality (C. Draxl, personal communication).

For the 3-year period of study (2013–15), we found a mean observed wind speed (1-min observations at the top of the hour) of 4.77 m s^{-1}, which is very close to the 4.85 m s^{-1} found by Draxl et al. [10] using the 5-min 80-m observations during the period 2007–12. We verified the 1-h HRRR forecasts for this period against the M2 observations using bilinear interpolation [10]. Fig. 3 shows the hourly M2 observations, HRRR 1-h forecasts, and the bias of the HRRR forecasts (HRRR forecast minus observation). A 30-d running mean is applied to smooth out the comparison. The HRRR exhibits a relatively constant positive bias of 0–1 m s^{-1} during the study period. The 1-h HRRR forecasts exhibit a wind speed mean bias of 0.65 m s^{-1} and a wind speed RMS error of 3.84 m s^{-1}; these numbers compare favorably with the bias of 0.95 m s^{-1} and RMS error of 4.24 m s^{-1} found by Draxl et al. [10] for the WIND Toolkit model during 2007–12.

To investigate the diurnal cycle of the HRRR wind speed bias at 80 m, we calculate a mean diurnal cycle of the verification statistics (Fig. 4). Fig. 4a shows that observed wind speeds reach their maximum in the afternoon hours; the HRRR 1-h forecasts generally reproduce this evolution, although the forecasted winds are too high, reaching a peak bias in the early morning. The RMS error remains relatively constant around 4 m s^{-1} during most of the day, but exhibits a relative minimum around midday (consistent with the behavior of the WIND Toolkit model [10]).

Since the NWTC facility is subject to frequent bursts of gusty winds and erratic mountain-wave-induced turbulence, particularly during the cool season, we believe that the M2 dataset represents one of the more challenging turbine-level wind verification datasets available. However, a comparison of HRRR 80-m wind forecasts with 100-m wind observations from a tall tower farther away from complex terrain (the Boulder Atmospheric Observatory near Erie, Colorado [17]) indicates generally consistent results (not shown). Verification of the HRRR forecasts using additional relatively unwaked tall tower measurements from other parts of the country would help to generalize these results; however, these datasets will

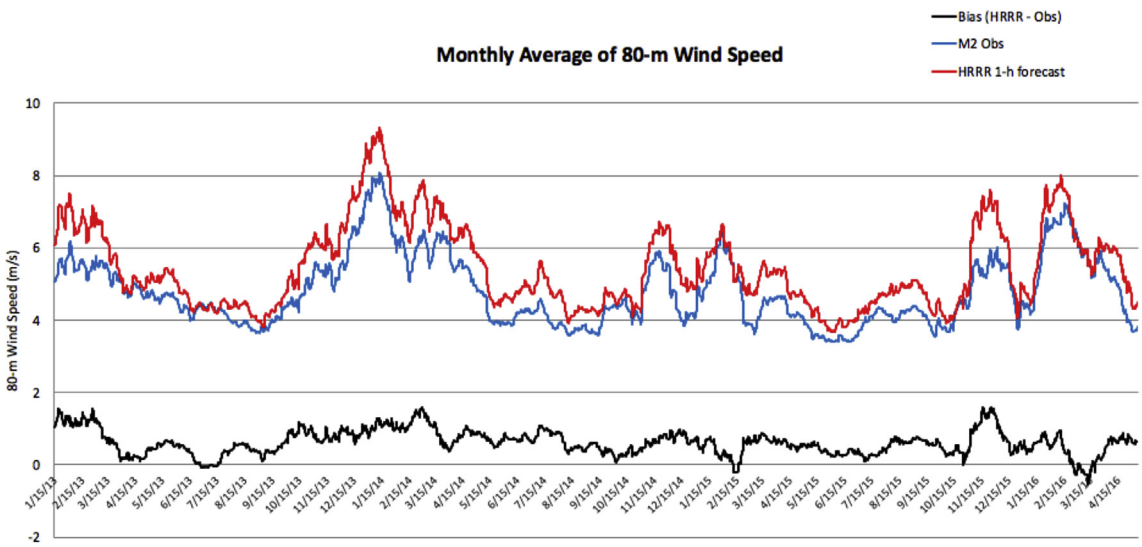

Fig. 3. 80-m wind speed observed (blue curve; m s^{-1}), forecasted by the HRRR with 1-h lead time (red curve; m s^{-1}), and bias (black curve; forecast minus observations; m s^{-1}) at the NWTC M2 tower (see text) during 2013–15. A 30-day running mean is applied to reduce the amount of short time-scale noise. (For interpretation of the references to colour in this figure legend, the reader is referred to the web version of this article.)

likely need to be quality-controlled, representing an effort beyond the scope of this preliminary work.

Intensive development work is ongoing within the RAP/HRRR development team to improve low-level wind forecasts, particularly through enhancements to the parameterization of planetary boundary layer (PBL) behavior; these efforts will continue to mitigate the high 80-m wind speed bias evident in Fig. 3.

2.4. Solar radiation verification

As mentioned above, high-quality solar radiation measurements are very sparse within the CONUS. In this section, we present some performance statistics for the HRRR as verified against measurements taken from the SURFRAD/ISIS networks [4]. The HRRR currently outputs only the shortwave irradiance components (direct, diffuse, and global horizontal).

Fig. 5a shows the downward shortwave irradiance RMS error and bias (forecast minus observation; W m^{-2}) averaged over all 14 of the SURFRAD/ISIS sites for HRRR 1-h forecasts. Obviously, there is an annual cycle in both forecast RMS error and bias since these metrics scale with the magnitude of the observed downward shortwave irradiance. Average biases reach up to about 40–50 W m^{-2} during the spring, and become as low as about 10–20 W m^{-2} in the autumn. Note that the average bias is always positive, indicating that the HRRR has deficient cloud cover and/or aerosol loading. Significant data assimilation and model physics improvements were implemented in the HRRR in early 2015, with many of them stemming from a DOE-sponsored Solar Forecast Improvement Project wherein the RAP/HRRR NWP system was evaluated for forecasts of solar irradiance with a view towards improving forecasts for solar energy users. The reduced bias in 2015 compared to previous years is attributed to these changes [6].

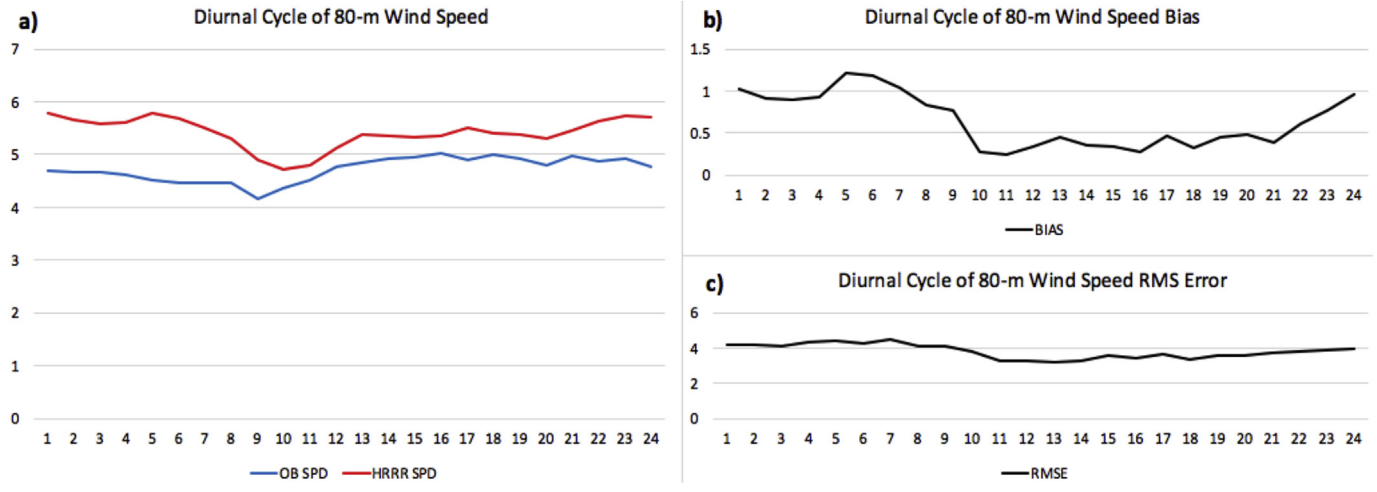

Fig. 4. Diurnal cycle of (a) observed (blue curve; m s^{-1}) and forecasted by the HRRR with 1-h lead time (red curve) 80-m wind speed (m s^{-1}), (b) 80-m wind speed bias (m s^{-1}), and (c) 80-m wind speed RMS error (m s^{-1}) at the NWTC M2 tower during the period 2013–15. All times are in local time (mountain standard time). (For interpretation of the references to colour in this figure legend, the reader is referred to the web version of this article.)

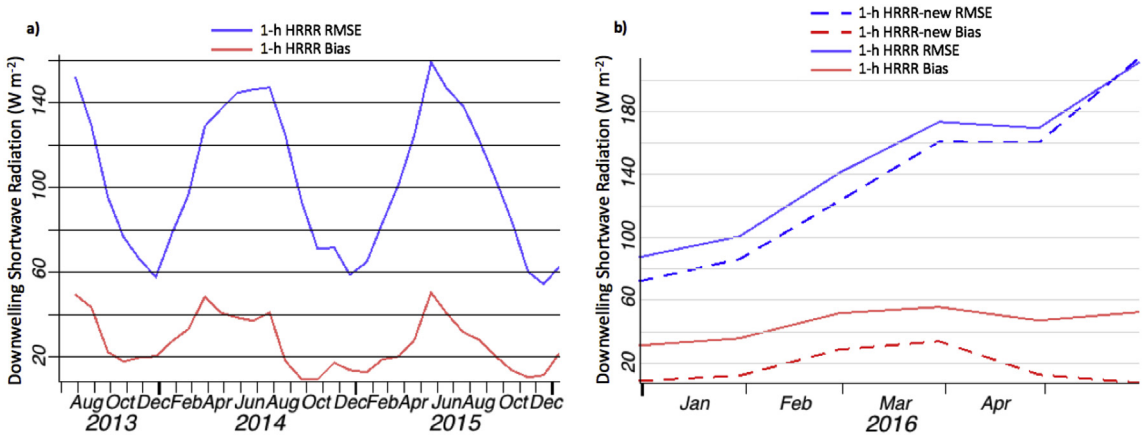

Fig. 5. Surface downward shortwave irradiance bias (red curves; forecast minus observation; W m^{-2}) and RMS error (blue curves; W m^{-2}) of (a) HRRR 1-h forecasts as verified against SURFRAD/ISIS measurements over the period 13 Jul 2013–31 Dec 2015, and (b) ESRL/GSD HRRR 1-h forecasts (solid lines) and 1-h forecasts from a parallel prototype version of the HRRR (dashed lines) over the period 1 Jan – 31 May 2016. (For interpretation of the references to colour in this figure legend, the reader is referred to the web version of this article.)

Fig. 5b shows verification from early 2016, plotting both the GSD HRRR and a more advanced prototype parallel version of the HRRR. This newest version of the HRRR, which will replace the prior version at ESRL/GSD in 2016, incorporates a more advanced treatment of subgrid-scale cloudiness using a mass-flux parameterization within the PBL scheme, and also includes a statistical cloud scheme capable of representing more general fractional cloudiness (including stratus and cirrus [8]).

3. Methodology

This study takes advantage of a three-year archive of HRRR forecasts. Our archive currently contains a large variety of 2-dimensional fields, both kinematic and moisture-related. For this study, only results related to the 80-m wind field and the surface downward shortwave irradiance are presented. While it is likely that wind fields at levels other than 80 m are of interest to the renewable energy community, at this time the HRRR forecast archive contains only the wind field at 10 and 80 m heights. Archival of the 3-dimensional HRRR forecast files would have permitted analysis at additional levels, but these files are prohibitively large by today's standards, and keeping multiple years on disk would not be practical at this point. Future years of the dataset will contain the radiation components, direct normal irradiance (DNI) and diffuse horizontal irradiance (DHI).

To calculate the summary long-term average fields presented in this study, the raw data are analyzed using a simple running calculation method. The 1-h forecasts are processed chronologically, keeping a record of sums and total number of forecasts for the calculations. An additional wind-related metric, useful for wind farm operators and utility managers, is the fraction of hours that the 80-m wind speed exceeds certain thresholds relevant to turbine operations. For this calculation, the procedure simply keeps a record of the number of "yes" exceedances of each threshold, and divides this number by the total number of forecasts, at each grid point. We use three thresholds of interest, guided by the typical power curves presented by Clack et al. [9]: 4 m s^{-1} (a point near the bottom of a typical power curve where only a small amount of power is generated from a wind turbine), 12 m s^{-1} (a point near the top of a typical power curve where the turbine is producing nearly maximum power), and 25 m s^{-1} (a point near the cut-out speed of a typical wind turbine's power curve). Fig. 6 shows these power curves as determined by Clack et al. [9]. The fraction of time that the 80-m wind speed exceeds these thresholds is potentially more useful to renewable energy users than the simple arithmetic average wind speed. Note that the specific values of the cut-in and cut-out speeds vary significantly among turbine models; our dataset is general enough to derive results for different wind speed thresholds.

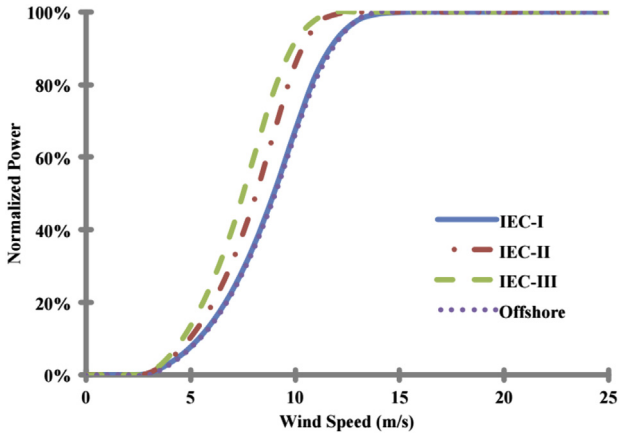

Fig. 6. Typical power curves (normalized power versus wind speed) derived by Clack et al. [9].

4. 80-m wind speed maps

In this section we present maps of 3-year average 80-m wind metrics.

4.1. CONUS overview

Fig. 7a shows the average 80-m wind speed from 1-h HRRR forecasts during the three years 2013–15. The average wind ranges between less than 4 m s^{-1} in some parts of Washington, Oregon, California, and western Mexico (as well as in sheltered valleys in the complex terrain of the interior western US) to nearly 10 m s^{-1} in the windiest regions (just offshore of Capes Blanco (Oregon) and Mendocino (California), in the higher ranges of the Rocky Mountains from northern New Mexico into British Columbia and Alberta, east of the Rockies from Colorado, Wyoming, and Montana to

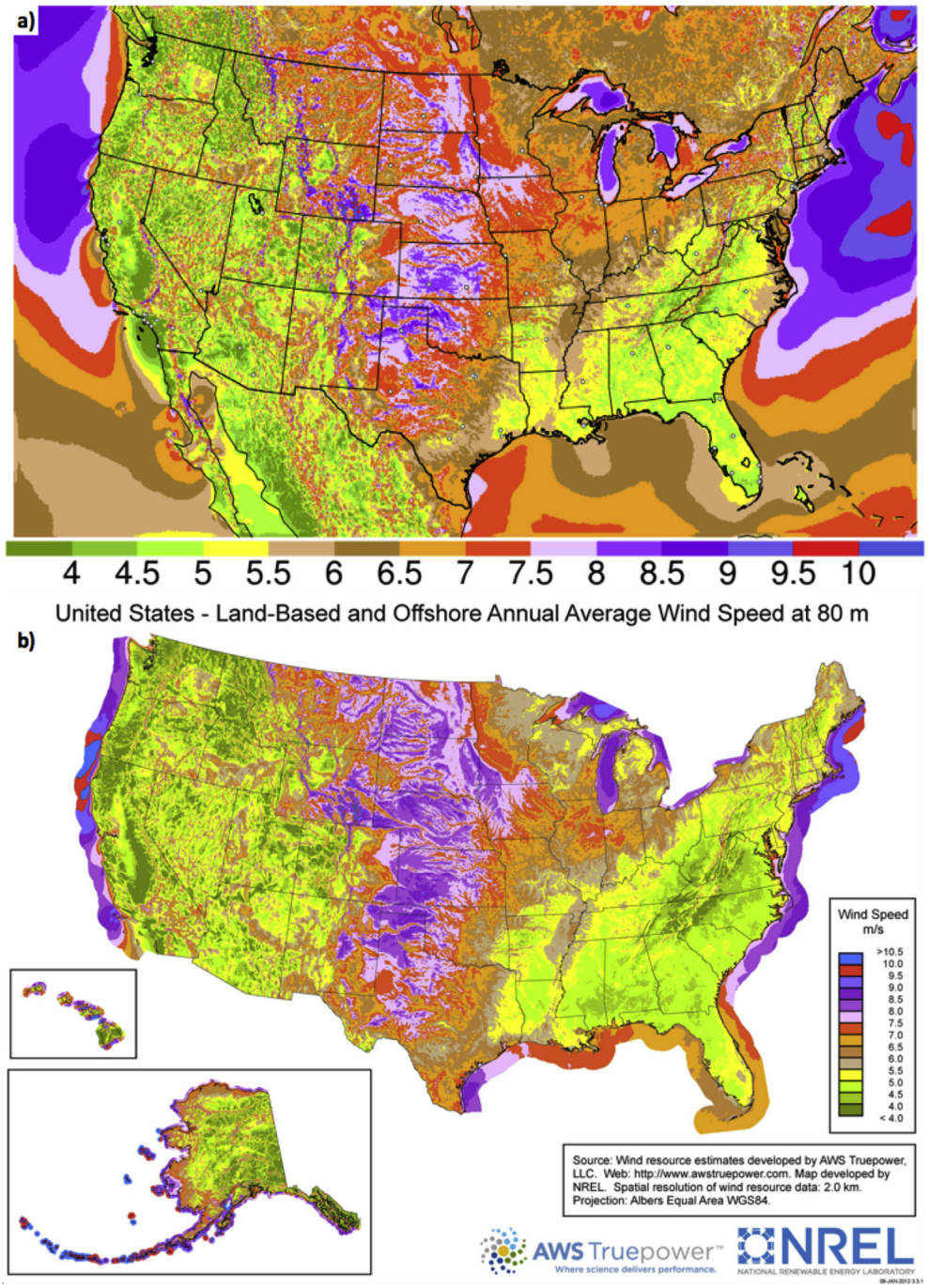

Fig. 7. (a) Average 80-m wind speed (m s^{-1}) from 1-h forecasts from the HRRR over the period 01 Jan 2013–31 Dec 2015; major airport hubs are identified by small white circles. (b) NREL average 80-m wind speed (m s^{-1}; [12]).

Alberta, in the Tehachapi Mountains of southern California, and in the mountains of Baja California Norte). In the eastern CONUS, and in the mountainous western CONUS, the highest average winds generally occur in areas of high terrain, with lighter average winds in the adjacent valleys and lowlands. The central CONUS clearly comprises the largest region of high average wind speed, at least over land. Even in the Great Plains, higher average winds are apparent along local ridges in the terrain. The offshore wind resource is very high both off the east and west coasts; however, engineering requirements dictate that most development so far has been off the east coast [23]. Note also that the Great Lakes (especially Superior) have relatively high mean wind speeds (greater than 8 m s^{-1}).

The average 80-m wind derived from the HRRR (Fig. 7a) can be compared with the same field calculated by NREL ([12]; our Fig. 7b), at least over the CONUS. The HRRR tends to have higher average 80-m wind speeds than the NREL dataset in most of the CONUS east of the Mississippi River; the HRRR is generally 0.5–1 m s^{-1} higher, but occasionally as much as 1.5–2 m s^{-1} higher. In the Plains states (particularly in the High Plains), however, the HRRR has lower average 80-m wind speeds than the NREL dataset (generally 0.5–1 m s^{-1} lower). Throughout the mountainous western CONUS,

the two datasets are more similar, although the HRRR appears to have higher maxima on the highest ridges. It is unclear how many of the differences seen here are due to the limited 3-year duration of our HRRR dataset, or a wind speed bias in HRRR 1-h forecasts at 80-m height (as described in Section 2.3). In general, the HRRR dataset shows strong overall similarity to the [12] graphic for US wind energy resource.

We can also compare the HRRR forecast dataset with the results from the WIND Toolkit ([10]; our Fig. 8) for one year of overlap (2013). The WIND Toolkit offshore wind speeds look more similar to the earlier [12] wind speeds, whereas over the southeastern CONUS the WIND Toolkit has much stronger winds than either the HRRR or the earlier NREL maps. Verification is difficult in this region due to the lack of elevated wind measurements.

Fig. 9 shows the exceedance frequency of the 4 m s^{-1} threshold from the HRRR dataset. This map further highlights the terrain dependence of the 80-m wind speed. Not many areas in the CONUS exceed this wind threshold more than 90% of the time, but there are some regions where it is exceeded during 85% of the 3-year study period. These include the eastern Pacific (off the coast of California), local ridges in the plains (particularly in the southern plains of Texas and Oklahoma), eastern Lake Superior, the Gulf Coast of south Texas, and the Atlantic coast. The 12 m s^{-1} threshold is exceeded much more rarely than the 4 m s^{-1} threshold (Fig. 10). Large portions of the southeastern CONUS and the west coast states exceed this threshold less than 5% of the time. Over-land regions exceeding this threshold more than 30% of the time are limited to ridges of high terrain in the Rockies, Appalachians, Cascades, Sierra Nevada, and the mountains of Baja California, and small portions of the high plains. Significant areas of the Great Lakes exceed the 12 m s^{-1} threshold over 15% of the time.

For completeness, we computed exceedance frequencies for a third threshold: 25 m s^{-1}, a typical cut-out speed for turbines to prevent damage, which is shown in Fig. 11. Note that the color scale

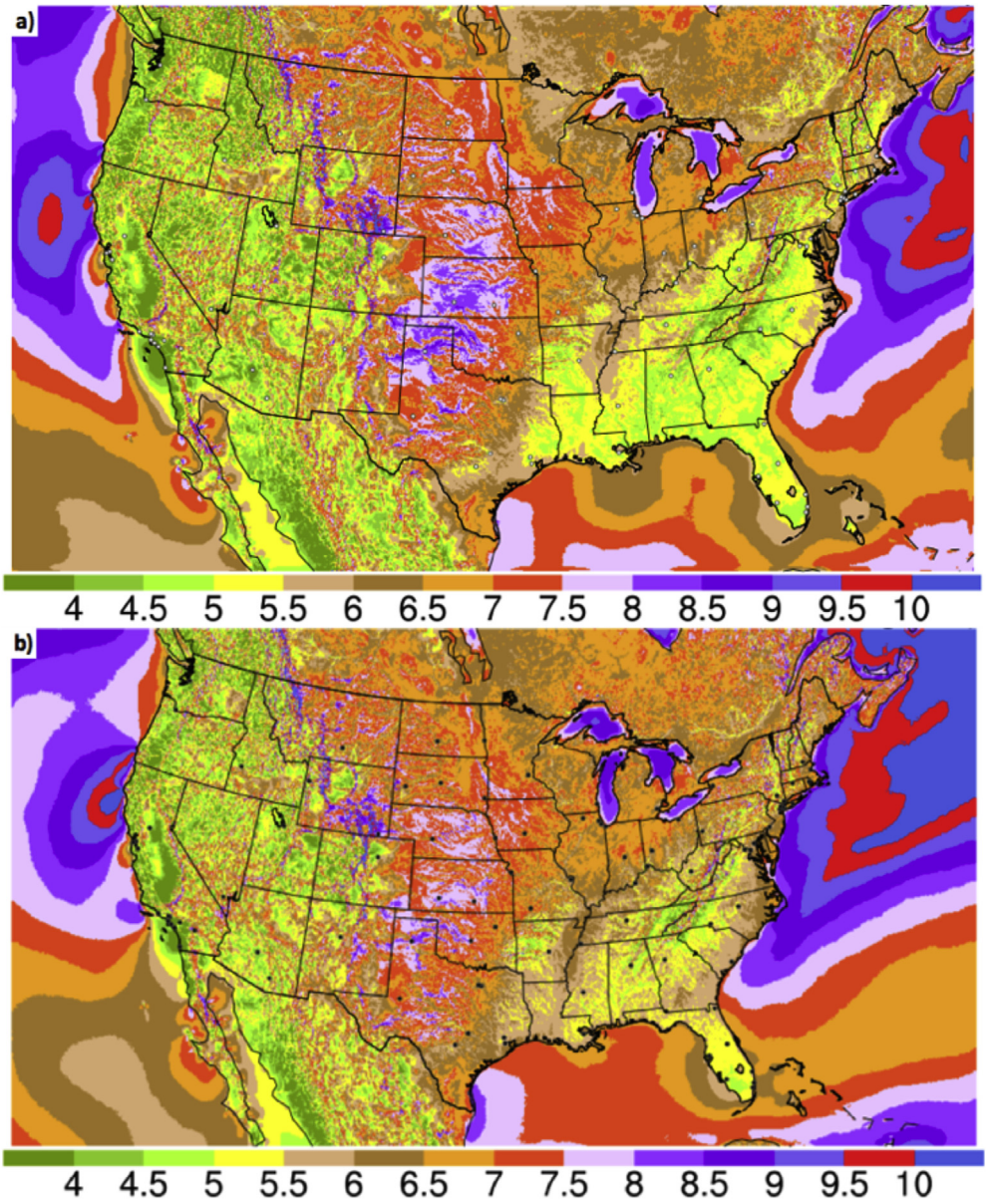

Fig. 8. (a) Average 80-m wind speed (m s^{-1}) from 1-h forecasts from the HRRR over the period 01 Jan – 31 Dec 2013; major airport hubs are identified by small white circles. (b) WIND Toolkit average 80-m wind speed (m s^{-1}) over the same period.

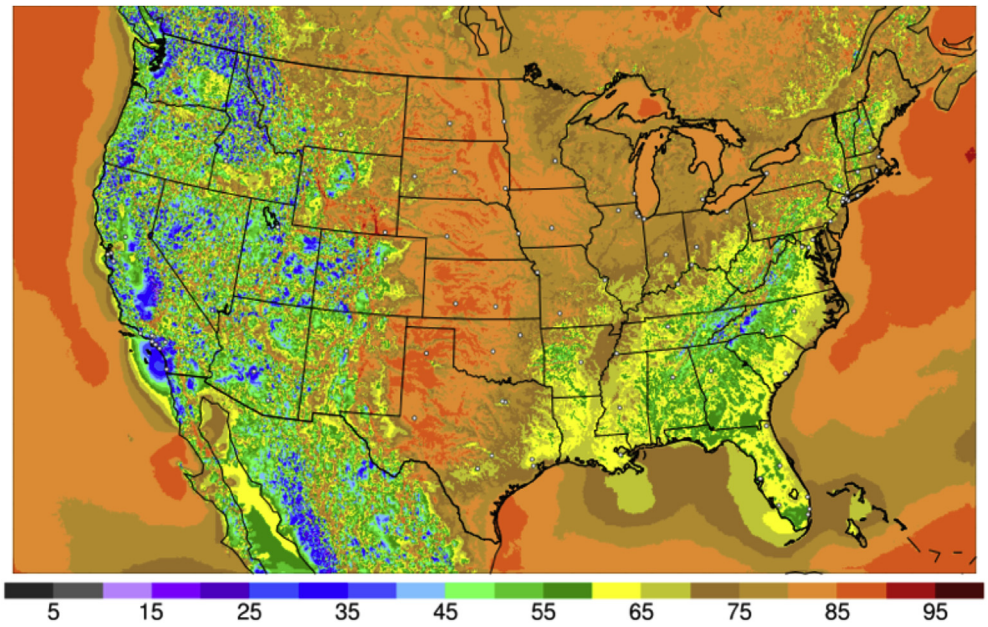

Fig. 9. Percent of time that the 80-m wind speed from the HRRR 1-h forecasts exceeds the threshold of 4 m s^{-1} over the period 01 Jan 2013–31 Dec 2015.

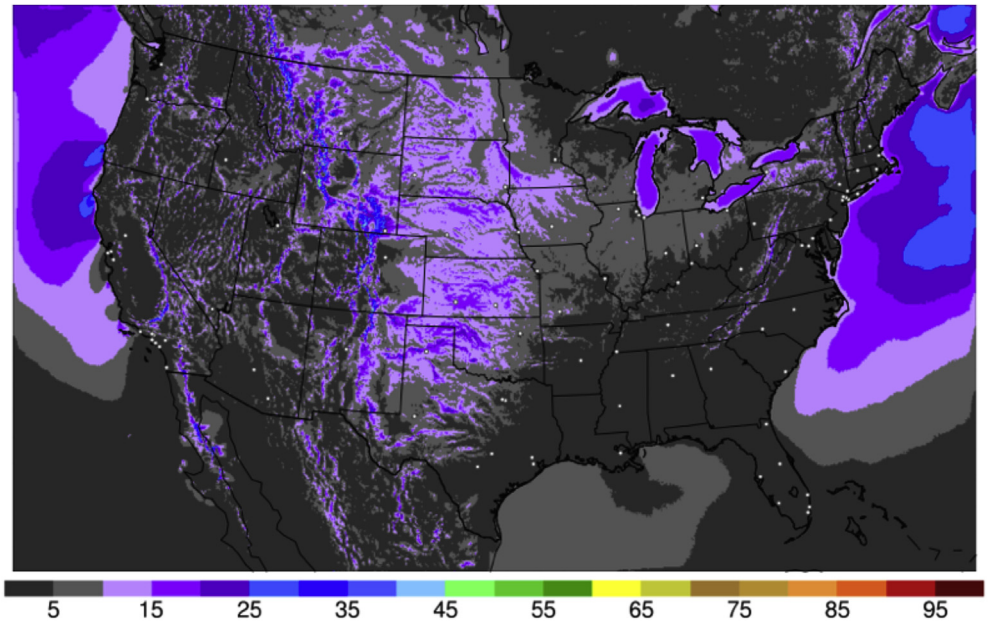

Fig. 10. As in Fig. 9, but for a threshold of 12 m s^{-1}.

is different in this map, with much lower values in order to highlight relative differences in frequency. Over most of the CONUS, the frequency of winds of this magnitude is less than 0.1%. Exceptions are the regions of high terrain in the western CONUS, the Nantucket and Cape Cod vicinity, the outer banks of North Carolina, and the area around Cape Blanco on the coast of Oregon. It is important to note that these frequencies may be highly variable from year to year. Since the frequencies are so low, they can be significantly affected by individual extreme events (such as tropical or extratropical cyclones). For example, the swath of higher frequencies off the west coast of Baja California is associated with the track of Major Hurricane Norbert, peaking in intensity on 6 Sep 2014. Some other regions of high frequency can similarly be traced to individual wind events. As the time period of our ongoing HRRR archive continues to lengthen, we expect that statistically significant geographic features will begin to emerge.

4.2. Great Plains wind corridor

As described in the previous section, the central plains of the CONUS are characterized by high average wind speeds, with stronger winds confined to subtle ridges of high terrain, and lighter winds occurring in lower river valley areas. Fig. 12 shows the difference between the exceedance frequencies of the 12 m s^{-1} threshold during the daytime and the nighttime. The daytime calculation includes all the HRRR 1-h forecasts valid from 15 to 00

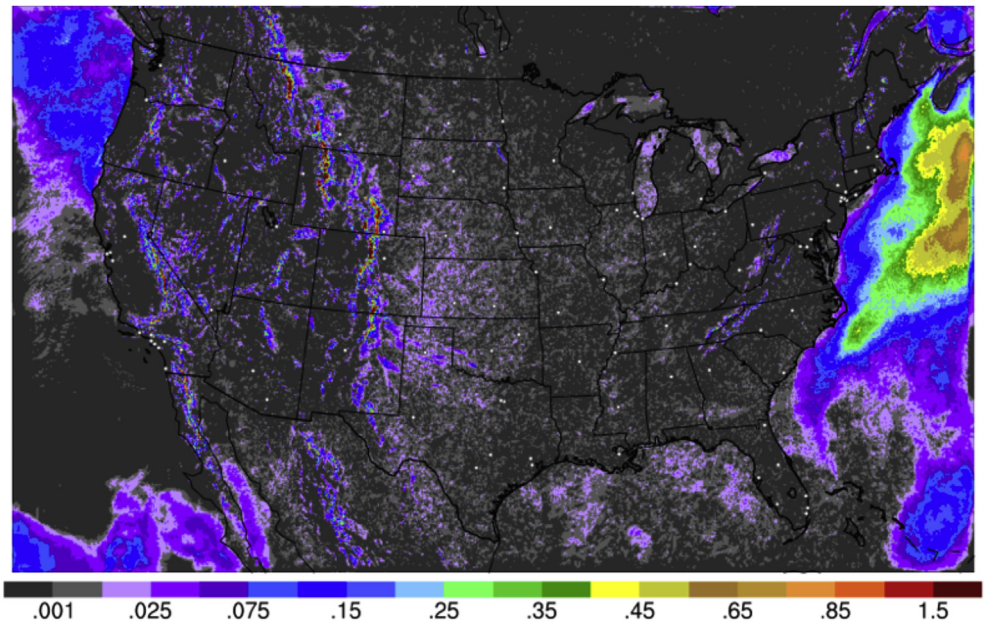

Fig. 11. As in Fig. 9, but for a threshold of 25 m s^{-1}.

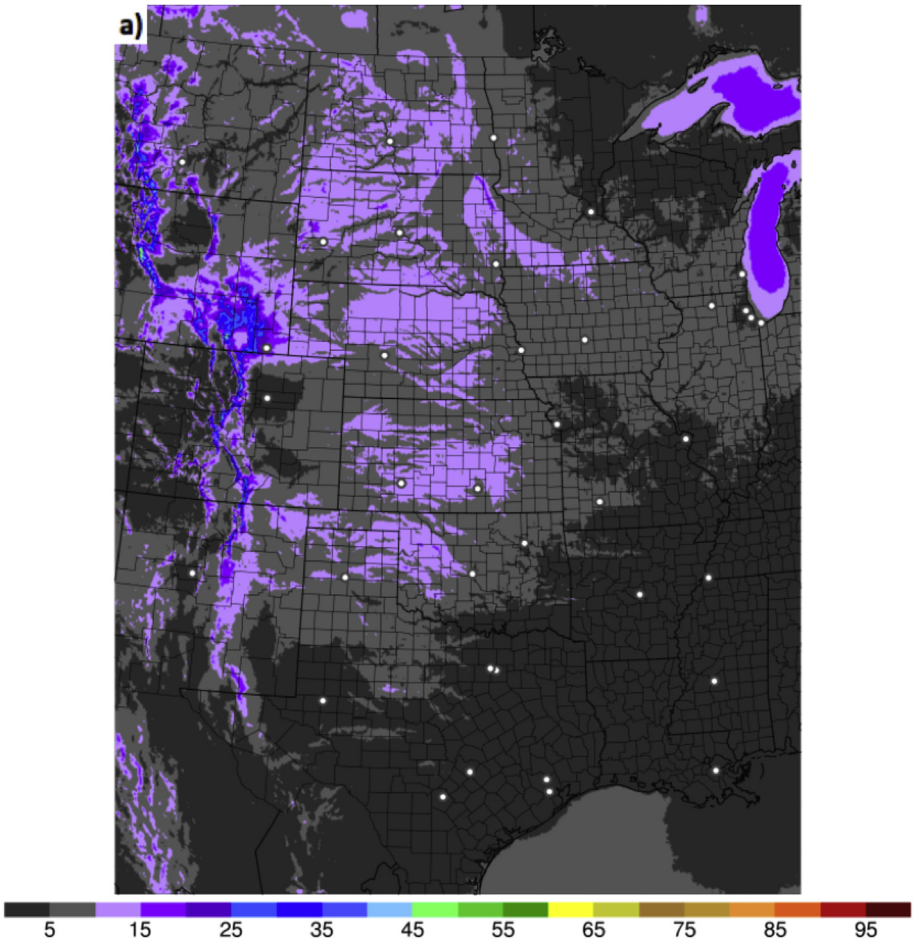

Fig. 12. (a) As in Fig. 10, but for the central plains only and showing diurnal variation. (a) Calculated during the daytime hours (1-h forecast valid times of 15-00 UTC). (b) Calculated during the nighttime hours (1-h forecast valid times of 03–12 UTC).

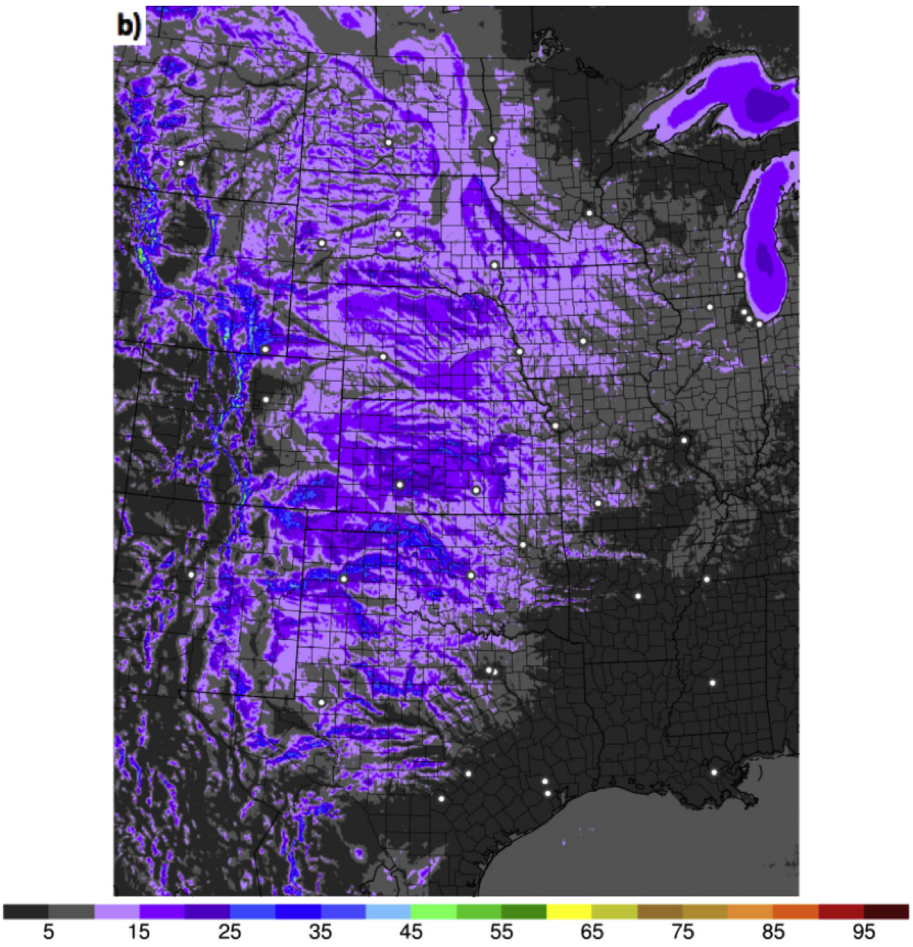

Fig. 12. (*continued*).

UTC (i.e., those initialized from 14 to 23 UTC; Fig. 12a), and the nighttime calculation includes all the HRRR 1-h forecasts valid from 03 to 12 UTC (i.e., those initialized from 02 to 11 UTC; Fig. 12b). The daytime valid hours cover 09–18 local time (LT; UTC − 6h) in the central CONUS time zone, and the nighttime valid hours cover 21-06 LT.

In the daytime, it is apparent that the gradients in the frequencies are quite small; the field is relatively smooth. There is a tendency for more frequent high winds at higher elevations. This result is physically logical, since the atmosphere is generally fairly well mixed during the daytime, but winds do gradually increase with elevation where high terrain intersects stronger mid-tropospheric winds. During the night, however, the field looks very different. The nighttime plot accentuates even the relatively small elevation differences that commonly exist in the plains. Local ridges of ~100 m higher elevation show up as having much more frequent high winds than local valleys. This is because the nocturnal boundary layer becomes decoupled from the surface, and a southerly low-level jet (LLJ) often forms nightly. Regions where the terrain protrudes up closer to the LLJ elevation naturally have higher 80-m winds than local valleys.

Many specific terrain features (some of which have been previously documented) show up as having frequent high winds. These include the Milk River Divide in southern Alberta, the Missouri Escarpment in western North Dakota, the Coteau des Prairies in eastern South Dakota and southwestern Minnesota, the Cheyenne Ridge of southeastern Wyoming and western Nebraska, the Raton Mesa of southeastern Colorado and northeastern New Mexico, the Gypsum Hills of western Oklahoma, the Caprock Escarpment in the Texas panhandle, and the Callahan Divide in northwestern Texas. These local ridges or escarpments in the terrain have more frequent high winds than the surrounding lowlands. The Cheyenne Ridge and the area to its west, sometimes referred to as the Wyoming wind corridor, appears particularly dominant in these maps, due to the fact that the prevailing westerlies are enhanced in this area as a result of terrain blocking by the high terrain of central Colorado [21]. Many of the terrain features described here have already been implemented into wind farm development plans.

4.3. Seasonal variability

In addition to the 3-year average statistics presented above, it is also possible to break down the results by season to examine the seasonal variability of the 80-m winds. For each of the 4 seasons, there are 3 years of HRRR forecast data. Winter is considered to be December-February (DJF; for this calculation we include Dec 2012 and exclude Dec 2015), spring March-May (MAM), summer June-August (JJA), and autumn September-November (SON).

Fig. 13 shows the CONUS mean 80-m wind speeds from the four seasons. In terms of offshore winds, the winter (Fig. 13a) is by far the windiest season offshore of the East Coast. At all times of year, there appears to be an elongated maximum in 80-m wind speed approximately aligned along the Gulf Stream. Off the West

Coast, the seasonal cycle is more complex. During the winter, the strongest winds are found in the far northwestern corner of the HRRR domain, several hundred miles offshore from Washington and British Columbia; this is likely related to the location of the midlatitude storm track. The emergence of a pronounced summertime wind speed maximum offshore of the northern California coast between Capes Blanco and Mendocino (Fig. 13c) is likely due to the seasonal shallowing of the marine layer and associated flow blocking by the relatively high Trinity Alps in far northwestern California; these mountains are much higher than the surrounding inland areas to the north and south. Smaller-scale wind speed maxima are seen year round just to the southwest of many capes along the coast, including Capes Blanco and Mendocino, and Points Arena, Sur, and Concepcion. Another year-round feature is a notable zone of light winds in the Southern California Bight. Note also that there are many interesting small-scale tip jets and wake features apparent along the west coast of Baja California; we hypothesize that the ones offshore are associated with island wakes and the related flow blocking phenomena occurring in stable stratification.

In the interior western CONUS, many valley locations actually have their strongest winds in the spring (Fig. 13b), with lighter winds during the other seasons. High terrain in the West, however, experiences strongest winds during the winter. This may be related to the fact that high terrain tracks more closely with jet stream activity (strongest in winter), but valley locations are more likely to be tied to surface cyclone activity (strongest in the spring in the intermountain region; [15]). The springtime mixed layer is also much deeper than in the winter, allowing stronger winds aloft to be mixed down to the surface.

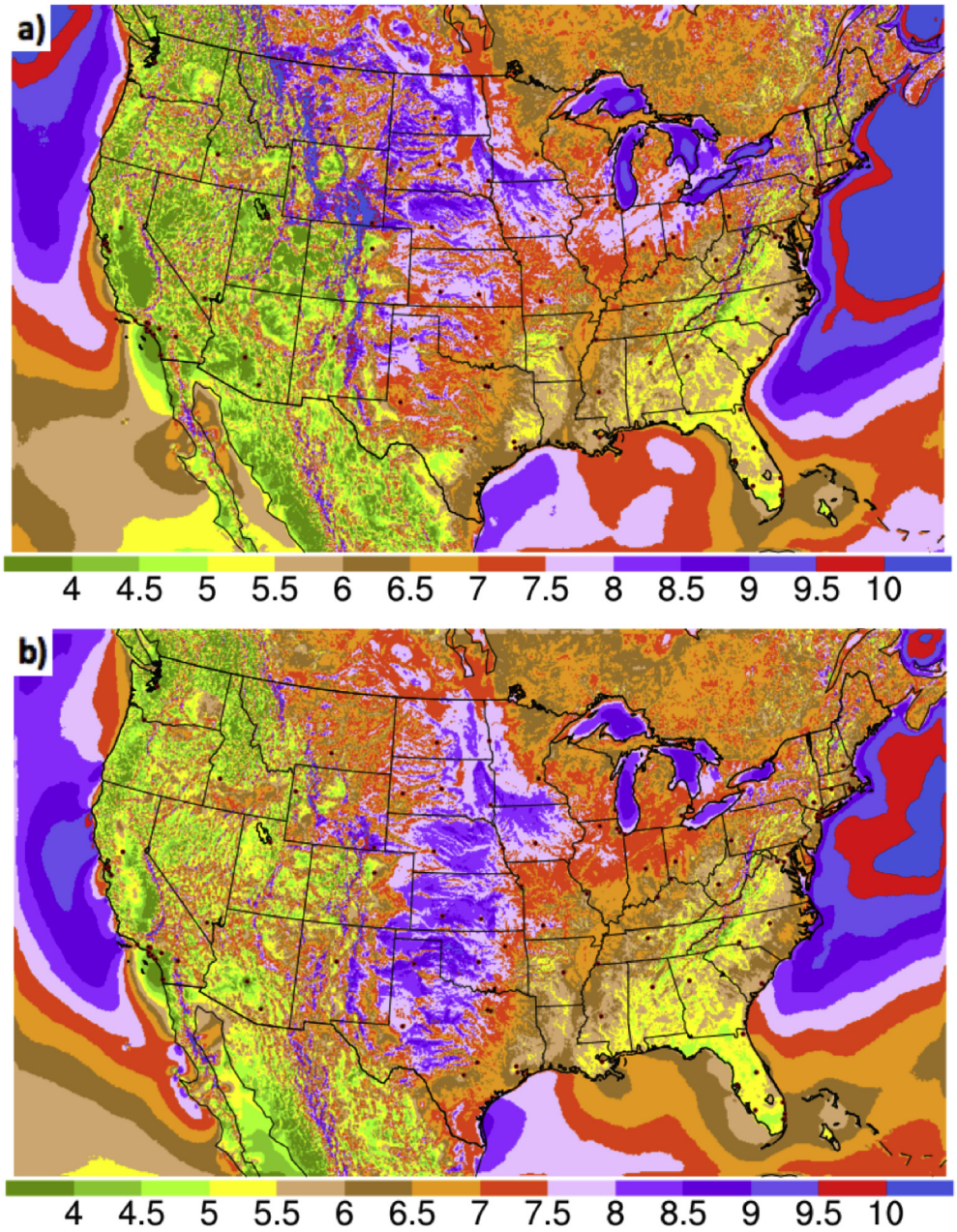

Fig. 13. Average 80-m wind speed (m s^{-1}) from 1-h HRRR forecasts over the periods (a) December–February (DJF) 2012–15, (b) March–May (MAM) 2013–15, (c) June–August (JJA) 2013–15, and (d) September–November (SON) 2013–15.

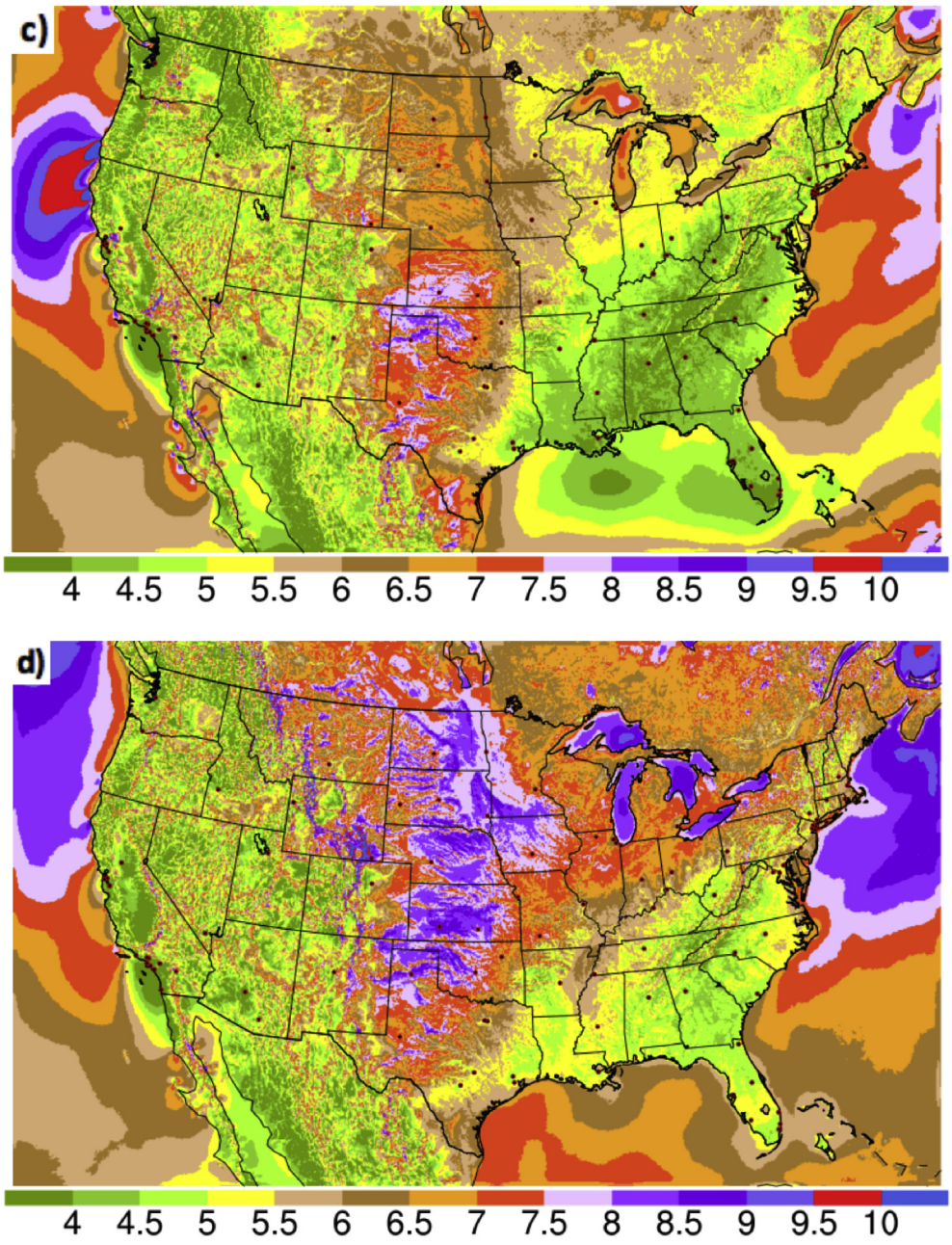

Fig. 13. (*continued*).

Over the plains states, the terrain dependence mentioned earlier (higher wind speeds on ridges, lower wind speeds in local valleys; Section 4.2) is seen at all times of year. However, there is a large latitudinal shift in the location of the strongest winds among the seasons. The strongest winds are seen in the transition seasons of spring and autumn. In winter, the maximum is in the far northern plains and northern high plains (central Montana and southern Alberta; Fig. 13a), whereas in the spring and summer, this shifts southwards to the southern high plains of Texas, Oklahoma, and Kansas. In the autumn, the maximum again begins to shift northwards, to the northern plains (especially the Dakotas and northern Nebraska).

Farther to the east, in the vicinity of the western Great Lakes, a corridor of higher 80-m wind speeds exists for most of the year (except in the summer). The latitude of the maximum wind speed shifts slightly north and south with the seasons, but this swath is generally through eastern Illinois and Wisconsin, southern Michigan, northern Indiana and Ohio, into southeastern Ontario. Wind speeds in the Appalachian Mountains show a strong seasonal cycle, with the strongest winds in the winter.

The existence of a multi-year meteorological dataset raises the question of whether the forecasted variable time series could be correlated with circulation indices for El Niño and other interannual oscillations. While this will be possible after we have archived many years of data, the brevity of our dataset precludes such an analysis at the moment. In the future, though, it should be possible to investigate the correlation of HRRR short-range wind and solar forecasts with the variation of circulation indices.

5. Solar radiation results

Operational NWP models are only recently beginning to output solar energy related variables, and model forecast evaluation for such irradiance fields is at an elementary stage (e.g., [16]). Fig. 14a shows the average incoming downward shortwave irradiance (which is similar, but not identical, to the global horizontal irradiance [GHI] due to GHI's inclusion of longwave irradiance) from hourly 1-h HRRR forecasts for the entire 3-year period. Note that averaging the entire period introduces many nighttime forecasts for which the downward shortwave irradiance is equal to zero; this reduces the averages everywhere. The spatial pattern of the average agrees reasonably well with prior expectations, and with gridded GHI fields calculated by NREL (Fig. 14b; [13]). Higher values occur in the desert southwestern CONUS, and relatively low values occur in the northern and eastern portions of the country. This is related to the climatological mean 500 hPa trough (and its associated cloudiness) over the eastern CONUS. The lowest values in the HRRR domain occur off the Pacific Northwest coast, associated with extensive cloud cover (both marine stratus and stratocumulus in the summer, as well as synoptic storm-related clouds during the cool season). The sharpness of the gradient in irradiance along the west coast is striking; sites just inland of the coast in southern California experience an average of 6–7 kW h m^{-2} $day^{-1,}$ while sites just off the coast receive less than 5.5 KWh m^{-2} day^{-1}. There are smaller gradients located near regions of high terrain; the rain shadow effect of the Cascades is particularly prominent.

Direct comparison between the NREL dataset and the HRRR is difficult, since both are based upon models and both have their inherent biases. However the relatively higher values in the HRRR

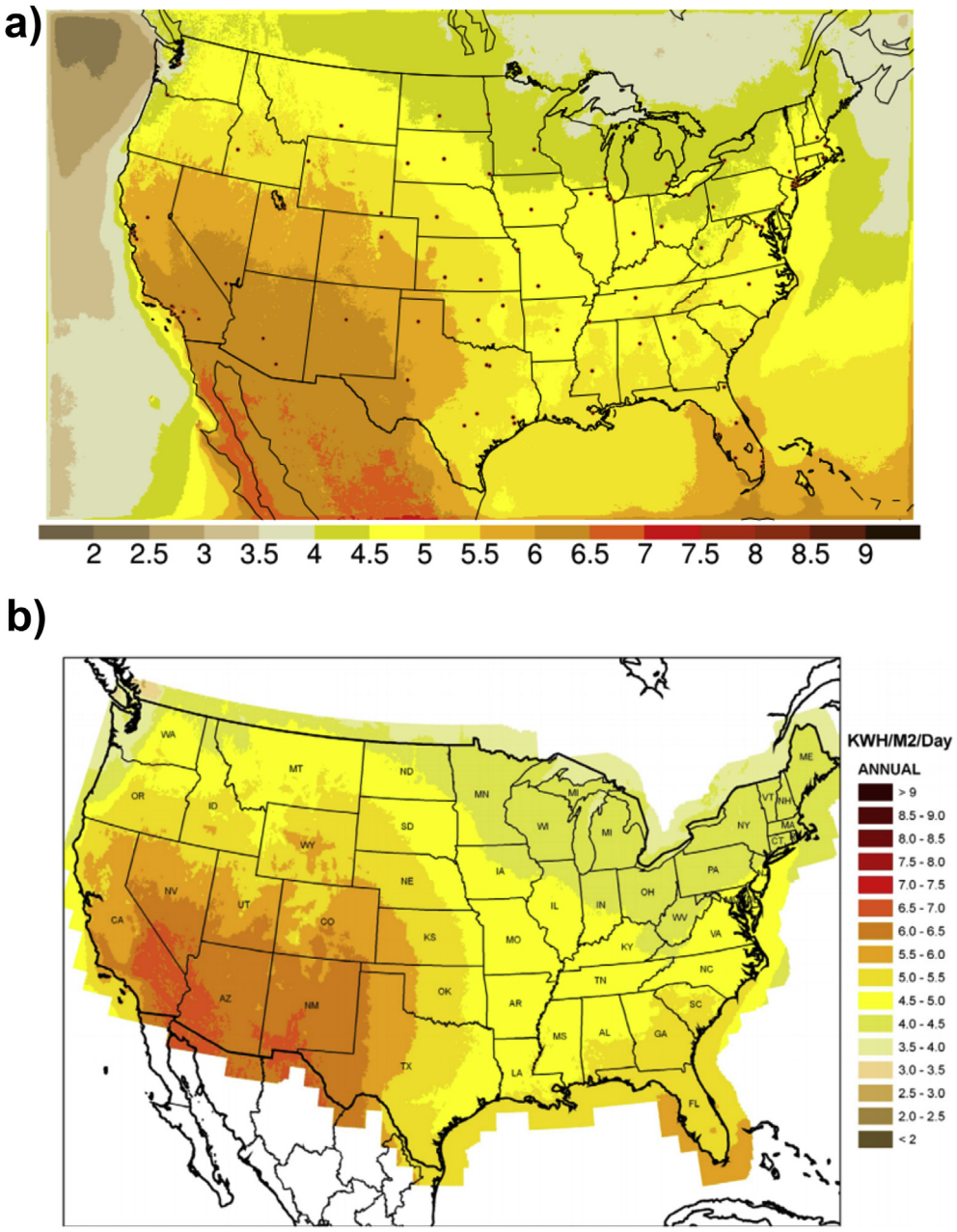

Fig. 14. (a) Average downward shortwave irradiance (KWh m^{-2} day^{-1}) from 1-h forecasts from the HRRR over the period 01 Jan 2013–31 Dec 2015; major airport hubs are identified by small white circles. (b) NREL NSRDB average downward shortwave irradiance (KWh m^{-2} day^{-1}).

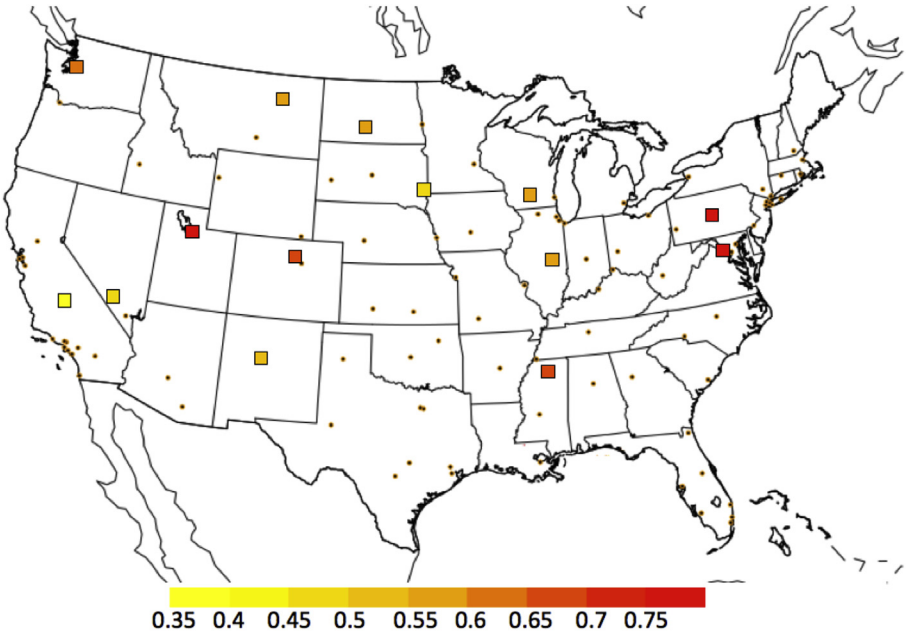

Fig. 15. Mean bias of HRRR 1-h forecasts of downward shortwave irradiance (KWh m^{-2} day^{-1}) as verified against SURFRAD/ISIS stations over the period Aug 2013 through Dec 2015. Major airport hubs are identified by small dots.

forecasts over most of the country (except for the interior southwestern US) agree qualitatively with the spatial pattern of HRRR forecast biases calculated against SURFRAD/ISIS stations (Fig. 15). Biases in HRRR forecasts are relatively low in the desert southwestern CONUS as well as the northern plains, while forecasts over the Pacific Northwest, the Intermountain West, and the eastern CONUS exhibit a more substantial high bias in incoming solar irradiance. Ongoing work is aimed at improving the representation of subgrid-scale cloud cover in the HRRR forecasts, which will improve irradiance forecasts (see section 2.4). Substantial model improvements for cloud and radiation forecasts have taken place during 2015–2016, and we anticipate additional further refinements in irradiance forecasts in future versions of the HRRR. In addition, radiation variables that are more useful to the industry (particularly direct normal irradiance [DNI]) are now being output in GSD's experimental HRRR, and are being archived for future analysis.

6. Conclusions

The dataset presented in this study fills a unique niche in the renewable energy community by providing meteorologically-consistent time-matched estimates of the wind and solar resource across the CONUS. The dataset has the added advantage of being derived from an advanced version of a widely-used NWP model.

Several shortcomings of the current dataset are currently being addressed to increase its applicability to renewable energy related problems. As mentioned above, additional important radiation variables are now being output by the HRRR, raising the possibility of future analysis of the variation and relationships between 80-m wind, GHI, and DNI. Also, the longevity of the archive continues to increase, providing greater statistical significance and a wider range of meteorological situations.

The wind and solar dataset from the HRRR is publically available. Additional information on the file formatting, as well as descriptions of the underlying NWP model configuration, is available at the website (http://rapidrefresh.noaa.gov/). The data itself, in GRIB2 format, is available via the Unidata THREDDs Data Server (TDS) interface (http://www.unidata.ucar.edu/software/thredds/current/tds/) at the following URL: (http://esrl.noaa.gov/gsd/thredds/catalog/data/retro/catalog.html). This dataset represents a starting point for further exploration of the relationships between wind and solar energy, and we anticipate the emergence of new applications of the dataset as well.

Acknowledgments

The authors would like to thank ESRL/GSD colleagues: Dr. Christopher Clack for his helpful comments and recommendations based on an earlier version of the manuscript, Brian Jamison for his help in setting up the scripts that carried out the running calculations, and Robert Lipschutz for his help in setting up public access to the dataset. Funding for this study was provided by the U.S. Department of Energy, Wind and Water Program, Award No. DE-EE0003080 and the NOAA ESRL Atmospheric Science for Renewable Energy Program.

References

[1] Alexander, C., S. S. Weygandt, S. Benjamin, D. C. Dowell, T. G. Smirnova, E. P. James, P. Hofmann, M. Hu, J. Olson, and J. M. Brown, 2014: The High-Resolution Rapid Refresh (HRRR): Updates to next-generation convective-scale forecast guidance with operational implementation in 2014. Paper presented at the 94th Annual Meeting of the American Meteorological Society, Atlanta, GA.

[2] American Wind Energy Association, AWEA U.S. Wind Energy Annual Market Report Year Ending, vol. 2012, 2013, p. 11.

[3] C.L. Archer, B.A. Colle, L. Delle Monache, M.J. Dvorak, J. Lundquist, B.H. Bailey, P. Beaucage, M.J. Churchfield, A.C. Fitch, B. Kosovic, S. Lee, P.J. Moriarty, H. Simao, R.J.A.M. Stevens, D. Veron, J. Zack, Meteorology for coastal/offshore wind energy in the United States: recommendations and research needs for the next 10 years, Bull. Amer. Meteor. Soc. 94 (2014) 515–519, http://dx.doi.org/10.1175/BAMS-D-13-00108.1.

[4] J.A. Augustine, G.B. Hodges, C.R. Cornwall, J.J. Michalsky, C.I. Medina, An update on SURFRAD—the GCOS surface radiation budget network for the continental United States, J. Atmos. Ocean. Technol. 22 (2005) 1460–1472, http://dx.doi.org/10.1175/JTECH1806.1.

[5] S.G. Benjamin, D.D. Devenyi, S.S. Weygandt, K.J. Brundage, J.M. Brown, G.A. Grell, D. Kim, B.E. Schwartz, T.G. Smirnova, T.-L. Smith, G.S. Manikin, An hourly assimilation-forecast cycle: the RUC, Mon. Wea. Rev. 132 (2004)

495–518, http://dx.doi.org/10.1175/1520-0493(2004)132<0495:AHACTR>2.0.CO;2.
[6] S.G. Benjamin, S.S. Weygandt, M. Hu, C. Alexander, T.G. Smirnova, J.B. Olson, J.M. Brown, E. James, D.C. Dowell, G.A. Grell, H. Lin, S. Peckham, T.-L. Smith, W.R. Moninger, G.S. Manikin, A North American hourly assimilation/model forecast cycle: the Rapid Refresh, Mon. Wea. Rev. 144 (2016) 1669–1694, http://dx.doi.org/10.1175/MWR-D-15-0242.1.
[7] J.A. Carta, S. Velázquez, P. Cabrera, A review of measure-correlate-predict (MCP) methods used to estimate long-term wind characteristics at a target site, Renew. Sustain. Energy Rev. 27 (2013) 362–400, http://dx.doi.org/10.1016/j.rser.2013.07.004.
[8] J.-P. Chaboureau, P. Bechtold, A simple cloud parameterization derived from cloud resolving model data: diagnostic and prognostic applications, J. Atmos. Sci. 59 (2002) 2362–2372.
[9] C.T.M. Clack, A. Alexander, A. Choukulkar, A.E. McDonald, Demonstrating the effect of vertical and directional shear for resource mapping of wind power, Wind Energy (2015), http://dx.doi.org/10.1002/we.1944.
[10] C. Draxl, A. Clifton, B.-M. Hodge, J. McCaa, The wind integration national dataset (wind) Toolkit, Appl. Energy 151 (2015) 355–366, http://dx.doi.org/10.1016/apenergy.2015.03.121.
[12] Elliott, D., M. Schwartz, S. Haymes, D. Heimiller, G. Scott, M. Brower, E. Hale, and B. Phelps, 2011: New wind energy resource potential estimates for the United States. Presentation at the Second Conf. on Weather, Climate, and the New Energy Economy, 27 Jan 2011, Seattle, WA.
[13] George, R., S. Wilcox, and M. Anderberg, 2008: National Solar Radiation Database (NSRDB) – 10 km gridded hourly solar database. Presentation at the Solar Resource Assessment Workshop, 29–30 Oct 2008, Denver, CO.
[14] D. Jager, A. Andreas, NREL National Wind Technology Center (NWTC): M2 Tower. NREL/DA-5500-56489, National Renewable Energy Laboratory, Golden, CO, 1996, http://dx.doi.org/10.5439/1052222.
[15] M.E. Jeglum, W.J. Steenburgh, T.P. Lee, L.F. Bosart, Multi-reanalysis climatology of intermountain cyclones, Mon. Wea. Rev. 138 (2010) 4035–4053, http://dx.doi.org/10.1175/2010MWRF3432.1.
[16] P.A. Jimenez, J.P. Hacker, J. Dudhia, S.E. Haupt, J.A. Ruiz-Arias, C.A. Gueymard, G. Thompson, T. Eidehammer, A. Deng, WRF-Solar: Description and clear-sky assessment of an augmented NWP model for solar power prediction, Bull. Amer. Meteor. Soc. 97 (2016) 1249–1264, http://dx.doi.org/10.1175/BAMS-D-14-00279.1.
[17] J.C. Kaimal, J.E. Gaynor, The boulder atmospheric observatory, J. Clim. Appl. Meteor. 22 (1983) 863–880.
[18] D.T. Kleist, D.F. Parrish, J.C. Derber, R. Treadon, W.-S. Wu, S. Lord, Introduction of the GSI into the NCEP global data assimilation system, Wea. Forecast. 24 (2009) 1691–1705, http://dx.doi.org/10.1175/2009WAF22222201.1.
[19] A.E. MacDonald, C.T.M. Clack, A. Alexander, A. Dunbar, J. Wilczak, Y. Xie, Future cost-competitive electricity systems and their impacts on US CO_2 emissions, Nat. Clim. Change 6 (2016) 526–531.
[20] M. Marquis, J. Wilczak, M. Ahlstrom, J. Sharp, A. Stern, J. Charles Smith, S. Calvert, Forecasting the wind to reach significant penetration levels of wind energy, Bull. Amer. Meteor. Soc. 92 (2011) 1159–1171, http://dx.doi.org/10.1175/2011BAMS3033.1.
[21] B.E. Martner, J.D. Marwitz, Wind characteristics in southern Wyoming, J. Appl. Meteor. 21 (1982) 1815–1827.
[22] F.M. Monaldo, X. Li, W.G. Pichel, C.R. Jackson, Ocean wind speed climatology from spaceborne SAR imagery, Bull. Amer. Meteor. Soc. (2014) 565–569, http://dx.doi.org/10.1175/BAMS-D-12-00165.1.
[23] W. Musial, Offshore wind: viable option for coastal regions of the United States, Mar. Technol. Soc. J. 41 (2007) 32–43.
[24] W. Musial, B. Ram, Large-scale Offshore Wind Power in the United States: Assessment of Opportunities and Barriers, NREL/TP-500-40745, National Renewable Energy Laboratory, Golden, CO, 2010.
[25] C.W. Potter, D. Lew, J. McCaa, S. Cheng, S. Eichelberger, E. Grimit, Creating the dataset for the western wind and solar integration study, Wind. Eng. 32 (2008) 325–328.
[26] D. Renné, R. George, S. Wilcox, T. Stoffel, D. Myers, D. Heimiller, Solar Resource Assessment, NREL/TP-581–42301, National Renewable Energy Laboratory, Golden, CO, 2008.
[27] M. Schwartz, D. Heimiller, S. Haymes, W. Musial, Assessment of Offshore Wind Energy Resources for the United States, NREL/TP-500-45889, National Renewable Energy Laboratory, Golden, CO, 2010.
[28] W.C. Skamarock, J.B. Klemp, J. Dudhia, D.O. Gill, D.M. Barker, M.G. Duda, X.-Y. Huang, W. Wang, J.G. Powers, A Description of the Advanced Research WRF Version 3, NCAR Tech. Note NCAR/TN-475+STR, 2008, p. 113.
[30] Solar Energy Industries Association, U.S. Solar Market Insight Report: 2013 Year-in-review, 2014, p. 20.
[31] U.S. DOE, Wind Vision: a New Era for Wind Power in the United States. U.S. Department of Energy Rep, DOE/GO-102015–4640, 2015, p. 289.
[32] U.S. DOE, 20% Wind Energy by 2030: Increasing Wind Energy's Contribution to U.S. Electricity Supply. U.S. Department of Energy Rep, DOE/GO-102008-2567, 2008, p. 248.
[34] S. Wilcox, National Solar Radiation Database 1991-2010 Update: User's Manual, NREL/TP-5500-54824, National Renewable Energy Laboratory, Golden, CO, 2012.
[35] T. Stoffel, A. Andreas, Solar Resource Measurements in Humboldt State University, Arcata, California, NREL/TP-5200-60425, National Renewable Energy Laboratory, Golden, CO, 2014.
[36] L.D. Riihimaki, F. Vignola, Establishing a Consistent Calibration Record for Eppley PSPs, Paper Presented at the 2008 SPIE Conference, San Diego, CA, 2008.
[37] W. Wendland, B. Scott, Measured Solar Radiation Over Illinois, Illinois State Water Survey, Champaign, IL, 2011, 14 pp.
[38] J. Kleissl, Solar Energy Forecasting and Resource Assessment, Associated Press, 2013, 416 pp.